

This is a postprint version of the following published document:

Martínez-Muriel, C. & Flores, O. (2020). Analysis of vortical gust impact on airfoils at low Reynolds number. *Journal of Fluids and Structures*, vol. 99, 103138.

DOI: [10.1016/j.jfluidstructs.2020.103138](https://doi.org/10.1016/j.jfluidstructs.2020.103138)

© 2020 Elsevier Ltd.



This work is licensed under a [Creative Commons Attribution-NonCommercial-NoDerivatives 4.0 International License](https://creativecommons.org/licenses/by-nc-nd/4.0/).

Analysis of Vortical Gust Impact on Airfoils at low Reynolds number

C. Martínez-Muriel¹ and O. Flores

Dept. Bioingeniería e Ing. Aeroespacial, Universidad Carlos III Madrid, Spain

¹Corresponding author: cayetano.martinez@uc3m.es

April 7, 2021

Abstract

The response of a NACA0012 airfoil impacted by vortical gusts is investigated performing Direct Numerical Simulations of the two-dimensional incompressible flow. Taylor vortices of different diameter and intensity located at different vertical separations with respect to the airfoil are deployed in the free stream. These vortices, which are characterized by its compact distribution of vorticity, are advected downstream to interact with the airfoil, set at a fixed angle of attack. For the low Reynolds number used in these simulations ($Re = 1000$), the effect of the different parameters defining the vortical gust and the impact is characterized. It is found that the change in the time evolution of the variation of the lift coefficient with respect to the steady state, $\Delta C_l(t)$, is fairly independent on the angle of attack, at least in the range of α considered in this study. Furthermore, it is found that the time at which the peak in ΔC_l is produced scales with the diameter of the viscous core of the vortex and the free-stream velocity, D/U_∞ . On the other hand, the maximum value of ΔC_l is roughly proportional to the non-dimensional vortex circulation, but varies non-linearly with the vertical distance between the vortex and the airfoil. This dependency can be captured by scaling ΔC_l with the relative intensity of the vertical velocity induced over the airfoil and the free-stream velocity (w_h/U_∞), where the former is defined as a integral of the vortex velocity profile over the chord of the airfoil. Using this scaling, the profiles of $\Delta C_l(tU_\infty/D)/(w_h/U_\infty)$ collapse over a single curve for the different vortex intensities, sizes and vertical separations considered in the present study, specially during the initial evolution of the vortical gust impact. The self-similar profile of $\Delta C_l(tU_\infty/D)/(w_h/U_\infty)$ is found to depend on the velocity profile of the vortex (i.e., Taylor vortices versus Lamb-Oseen vortices). However, the peak aerodynamic force and the time to peak aerodynamic force seem to scale with D/U_∞ and w_h/U_∞ irrespective of the velocity profile of the vortex, suggesting that our definition of w_h is sufficiently robust.

1 Introduction

Unsteady aerodynamics, and in particular the unsteady response of airfoils to gusts, has been thoroughly studied in the frame of potential flow. The literature in the topic is vast, including classical [14, 26, 11] and more recent works [28, 27, 8], among many others. In general, the applications of potential theory to the gust response of an airfoil is a simplification of the problem that requires several assumptions, including a sufficiently high Reynolds number, attached flow over the airfoil and considering the gust as a small perturbation compared to the free stream. The conditions that allow these assumptions are easily satisfied in most conventional aircraft, but they are not easily satisfied for Micro Air Vehicles (MAVs).

According to [20], MAVs are small aerial vehicles with characteristic wing span of the order of 15 cm and cruise speeds of 1-10 m/s. Using Kolmogorov's scaling for an equilibrium turbulent flow, it is easy to show that in a typical atmospheric boundary layer the velocity fluctuations associated with a length scale of the order of $O(0.1)$ m are of the order of

$O(1)$ m/s. This results in a gust velocity comparable to the cruise speed of the MAV, invalidating the small perturbation hypothesis and often resulting in massive separated flow over the wing of the MAV. Moreover, the typical Reynolds number of conventional aircraft is $Re = U_\infty c / \nu \sim 10^6 - 10^8$ (where c is the characteristic chord of the wing, U_∞ is the free-stream velocity and ν is the kinematic viscosity of air), while the Reynolds numbers for MAVs are usually much smaller, $Re \sim 10^3 - 10^5$.

The difference in the velocity and length ratios (i.e., between the gust and the vehicle) of conventional aircraft and MAVs has consequences in terms of the applicability of the different gust models that can be found in the literature. For a conventional aircraft a typical gust consists of a small velocity perturbation (longitudinal or transverse) occurring over a length scale much larger than the airfoil chord. These gusts can be modelled by an appropriate surge, plunge or pitching motion of the airfoil, since the velocity perturbation is felt (roughly) at the same time over the whole airfoil. Examples of recent studies of this type of gust at moderate to low Reynolds numbers include [25] and [19], among others. The results show that the gust produces a transient increase in the aerodynamic forces associated to the changes in the effective angle of attack of the plate, followed by an opposite sign extremum of smaller amplitude associated to the deceleration of the flow displaced by the plunge motion of the airfoil.

For MAVs, the small size of the vehicle results in a localized gust, where the characteristic length of the velocity perturbation is of the same order of magnitude (or even smaller) than the chord of the airfoil. Most experimental and numerical realization of these types of gusts are based on either airfoils/wings passing over a vertical jet (i.e., localized transverse gusts as in 24, 6, 15, 9), or airfoils/wings encountering a localized vortex in the free-stream (i.e., vortical gusts as in 12, 4, 30, 1, 22, 21, 5, 7). The results of the localized transverse gusts are very similar to the plunge manoeuvres discussed earlier when the jet width is sufficiently large [15, 9]. For narrower jets, the initial evolution and the maximum lift coefficient are still similar to those observed in the plunge manoeuvres, but the interaction of the leading edge vortex with the trailing shear layer of the jet results in a different recovery of the aerodynamic forces.

Note that plunge manoeuvres and localized transverse gusts (jets) are inherently different to the vortical gusts, since in the latter the vortex intensity is modified by the interaction with the airfoil. Also, the vertical velocity induced by the vortex on the airfoil changes sign as the vortex moves downstream, resulting in two extrema of opposite sign on the lift coefficient with comparable intensities. The results of [4, 22, 21] at moderate Reynolds numbers ($Re \sim 10^3 - 10^4$) show that the times and intensities of these extrema depend on the intensity, size and vertical displacement of the vortex with respect to the airfoil. Similar conclusions are offered by [1], who propose a potential model to predict the lift force produced by a vortical gust. The model shows a moderately good agreement with the experimental results when the vertical distance between the vortex and the airfoil is sufficiently large, failing to predict head-on collisions. The potential model predicts that the enhancement of the aerodynamic forces is proportional to the vortex circulation and to the relative velocity between the vortex and the airfoil, producing a maximum force when the vortex trajectory bifurcates from passing above to below the airfoil.

It should be noted that the vortices generated in the experiment of [1] have viscous cores much smaller than the airfoil chord, so that the non-linear interactions between the airfoil and the incoming vortex are restricted to the trajectory of the vortex. On the other hand, the experiments of [12, 22] and the numerical simulations of [4, 30, 21] have larger viscous cores, of the order of 0.1 - 0.5 chords. Larger viscous cores allow for stronger non-linear interactions between the vortex and the airfoil, specially for near head-on collisions, where the airfoil splits the vortex, disturbing the upper and lower boundary layer over the airfoil [4].

A second important difference between the aforementioned studies is the velocity profile of the vortical gust. While [1, 30] report vortical gusts with potential-like vortices (i.e.,

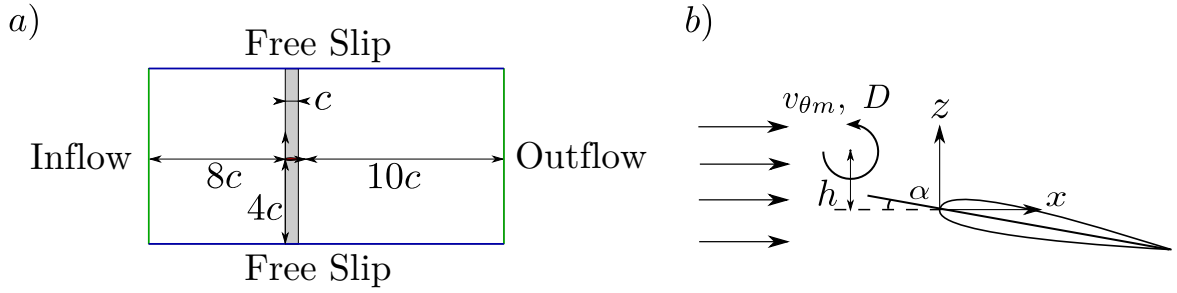


Figure 1: (a) Sketch of the computational domain. Grey zone represents the location of the airfoil in the x direction. (b) Sketch for the initial condition with the vortical gust.

with circumferential velocities decaying as the inverse of the distance to the vortical core), [21, 4, 5] use Taylor vortices. The slower decay of the circumferential velocity of the former allow larger-scale interaction between the vortical gust and the airfoil, which potentially can affect the trajectory of the vortex and the maximum aerodynamic forces produced during the interaction.

The purpose of the present study is to analyze the aerodynamic performance of airfoils in the presence of large vortical gusts at low Reynolds numbers, of the order of $Re \sim 10^3$. The vortex sizes and characteristic velocities considered in this study are of the order of the free-stream velocity and the airfoil chord, respectively. As a consequence, the study corresponds to the flight regime of the smaller MAVs, which has not been covered in previous studies. The effect of the vortex size, intensity and vertical displacements will be analyzed, as well as the effect of decay rate of the circumferential velocity of the vortex. **To that end, Taylor vortices and Lamb-Oseen vortices will be used to model vortical gusts. These two type of vortex models have very different profiles of circumferential velocity, and both have been used in the literature to model numerically vortical gusts (i.e., Lamb-Oseen vortices in [30], Taylor vortices in [21, 4, 5]).**

The paper is organized as follows. The details of the numerical method are described in section 2. In section 3, the results for Taylor-vortex gusts impact on a NACA0012 are presented, where the response of the airfoil is characterized in terms of flow and forces. We extend the analysis to the rest of the cases in the database (Taylor and Lamb-Oseen vortices) and compare the obtained results with those provided by the potential theory. To end with the section, a semi-empiric model for the aerodynamic response of the airfoil is developed. Finally, conclusions are presented in section 4.

2 Numerical Method

The two-dimensional Navier-Stokes equations for an incompressible flow are solved using Direct Numerical Simulation (DNS) to evaluate the performance of a NACA0012 airfoil at angle of attack α when it encounters a vortical gust. The Reynolds number based on the airfoil chord c and the free stream velocity U_∞ is $Re = cU_\infty/\nu = 1000$, where ν is the kinematic viscosity of the fluid. Different velocities and sizes are considered for the vortical gust, which is modeled with a viscous vortex as discussed below.

The DNS is performed using TUCAN, a finite differences code with an immersed boundary method. For the temporal discretization, TUCAN uses a three-stages semi-implicit low-storage Runge-Kutta scheme. The spatial derivatives are approximated by centered finite differences in a staggered grid. The implementation of the immersed boundary method is the direct forcing proposed by [29], using a regularized delta with a 3-point stencil. TUCAN has already been extensively validated, both for 2D [17, 18] and 3D [10, 2, 3] configurations. More details about the implementation of TUCAN in 2D can be found in [16].

The simulations have been performed in the computational domain sketched in figure 1a,

with dimensions $19c \times 8c$ in the streamwise and vertical directions, respectively. As shown in the figure, the airfoil is located roughly in the middle of the computational domain, leaving enough space upstream to place the viscous vortex that models the gust, and enough space downstream to properly develop the wake. The origin of the reference system is located at the leading edge of the airfoil. The free stream condition is modeled with an inflow velocity at the inlet boundary (left), while the outflow has been modeled with an advective boundary condition ($\partial \mathbf{u} / \partial t + U_\infty \partial \mathbf{u} / \partial x = 0$) at the outlet (right). Free slip boundary conditions are imposed in the horizontal boundaries (top and bottom).

The spatial resolution used for this study is 128 points per chord, which was selected after a grid refinement study. This spatial resolution yields a total of 2432×1024 grid points in the streamwise and vertical directions, respectively. The temporal resolution is chosen such that $CFL \leq 0.25$.

The vortical gust is modelled as viscous vortex, initially placed in the free stream at $x_0 = -4c$ (i.e. 4 chords upstream of the leading edge) and $z_0 = h$, as shown in figure 1b. Two different vortex models are considered in the present study. Most cases presented here use finite Taylor vortices, like the ones used in [4, 21]. They have a characteristic diameter D , a characteristic circumferential velocity $v_{\theta m}$, and a circumferential velocity distribution given by

$$v_\theta = -v_{\theta m} \frac{2r}{D} \exp\left(\frac{-2r^2}{D^2}\right), \quad (1)$$

$$r = \sqrt{(x - x_0)^2 + (z - z_0)^2}. \quad (2)$$

This velocity profile is plotted in figure 2, together with the corresponding distribution of vorticity. It can be observed that the circumferential velocity is maximum at $r/D = 1/2$, where the circulation becomes $\Gamma = \Gamma_{v_{\theta m \max}} = \pi \exp\{-1/2\} v_{\theta m} D$. Besides, the vorticity distribution changes sign at $r/D = 1/\sqrt{2}$. At this radius the circulation of the viscous vortex is maximum, and equal to $\Gamma_{\max} = 2\pi \exp\{-1\} v_{\theta m} D$.

The present study also includes a few cases with Lamb-Oseen vortices. The rationale for this is to evaluate the effect that the vortex velocity profile has on the aerodynamic forces developed in the airfoil. Lamb-Oseen vortices have

$$v_\theta = \frac{\Gamma}{2\pi r} \left[1 - \exp\left(\frac{-4r^2}{D^2}\right) \right], \quad (3)$$

whose center will be initially located at $x_0 = -6c$. These simulations are run in a larger computational domain, with the inlet plane located at $-12c$. The vorticity and velocity profiles of this vortices are compared to Taylor vortices in figure 2, showing a similar viscous core but a much slower decay of the circumferential velocity. Indeed, at $r \gtrsim D$ the velocity of the Lamb-Oseen vortices is indistinguishable from that of potential vortices with comparable circulation, as shown in the figure.

3 Results

The effect that a vortical gust (with a given v_θ profile) has on the aerodynamic forces on a given airfoil depends on 4 parameters: the angle of attack of the airfoil (α), the size (D) and intensity ($v_{\theta m}$) of the vortex, and its vertical location (h) with respect to the leading edge of the airfoil. The influence of these parameters is analyzed with a parametric study, considering all combinations of 3 values for each parameter:

$$v_{\theta m} / U_\infty = 0.1, 0.3, 1.0 \quad (4)$$

$$D/c = 0.5, 1.0, 2.0 \quad (5)$$

$$h/c = 0.0, 0.5, 1.0 \quad (6)$$

$$\alpha = 0^\circ, 8^\circ, -8^\circ. \quad (7)$$

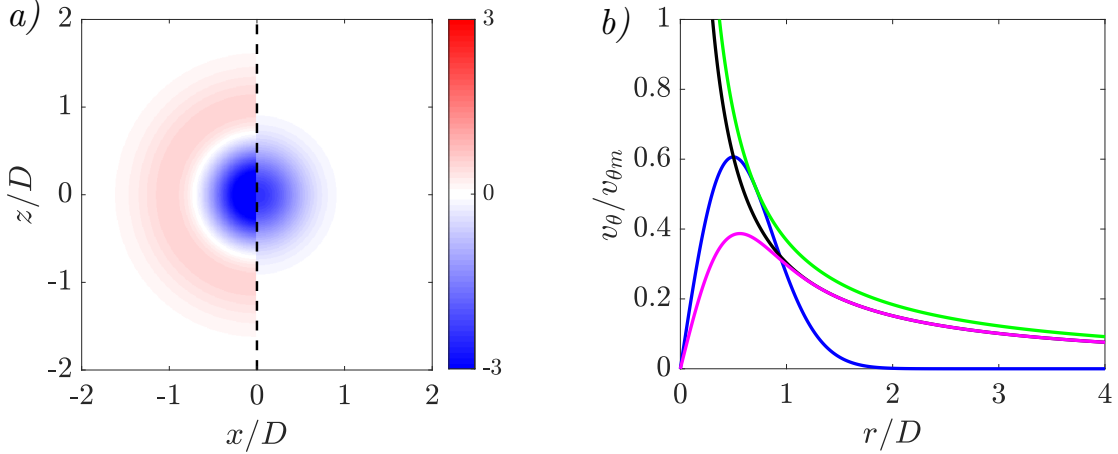


Figure 2: (a) Normalized vorticity, $\omega D/v_{\theta m}$, for viscous vortices: Taylor vortex (eq. 2) at the left, Lamb-Oseen vortex (eq. 3) with $\Gamma = \Gamma_{v_{\theta_{max}}} = \pi \exp\{-1/2\}v_{\theta m}D$ at the right. (b) Normalized circumferential velocity profiles of viscous and potential vortices. —: Taylor vortex. —: Lamb-Oseen vortex with $\Gamma = \Gamma_{v_{\theta_{max}}}$. —: Potential vortex with $\Gamma = \Gamma_{v_{\theta_{max}}}$. —: Potential vortex with $\Gamma = \Gamma_{max} = 2\pi \exp\{-1\}v_{\theta m}D$.

This results in a database of 81 simulations, for Taylor vortices, with a few additional cases using Lamb-Oseen vortices, available at <http://aero.uc3m.es/cfd.html>. In the following, these cases are labeled as $AaZzDdVv$, where a represents the angle of attack α , z is the nondimensional initial vertical position of the vortical gust h/c , d stands for the diameter of the core of the vortex normalized with the chord D/c , and v is the circumferential velocity of the vortex normalized with the freestream velocity $v_{\theta m}/U_{\infty}$. For example, A0Z0D1V1 stands the case were the airfoil with angle of attack $\alpha = 0^{\circ}$ is impacted by a vortex with intensity $v_{\theta m}/U_{\infty} = 1$ and size $D/c = 1$, initially located at a vertical distance $h/c = 0$ with respect to the leading edge of the airfoil.

Note that, unless explicitly stated, the results presented in this section correspond to Taylor vortices.

3.1 Effects on C_l and C_d

We first describe the evolution of the flow around the airfoil during the impact of the vortical gust, prior to analyze the effect on the aerodynamic forces (i.e, lift and drag coefficients). Figure 3 shows the instantaneous vorticity field around the airfoil at several times. The time reference ($t = 0$) is taken as the time when the center of the vortical gust would have reached the leading edge of the airfoil ($x = 0$) if the airfoil were not present. Positive/negative vorticity (i.e., clockwise/counterclockwise) is represented in red/blue colors in the figure. The green line upstream of the airfoil shows an instantaneous streamline arriving to a point located $0.1c$ upstream of the leading edge of the airfoil, and serves as an indicator for the effective angle of attack of the airfoil. The figure also includes contours of the Lambda-2 vortex identification method of [13], using a threshold $\lambda_2 = -0.25U_{\infty}^2/c^2 \approx -4 \times 10^{-4}\omega_{max}^2$.

Figures 3a and b show that as the vortical gust approaches the airfoil, it induces a positive effective angle of attack. This increase in the effective angle of attack results in the formation of a Leading Edge Vortex (LEV) in the upper surface of the airfoil, which travels downstream over the surface of the airfoil (figure 3c, d and e). At the same time, the boundary layer in the lower surface of the airfoil becomes thinner, and the stagnation point at the leading edge of the airfoil moves towards the lower surface. As the vortical gust moves around the airfoil, the effective angle of attack changes sign, the stagnation point in the leading edge shifts towards the upper surface, and the boundary layer in the lower surface becomes thicker. By the time the vortical gust leaves the airfoil (figure 3f), the LEVs formed in the upper surface

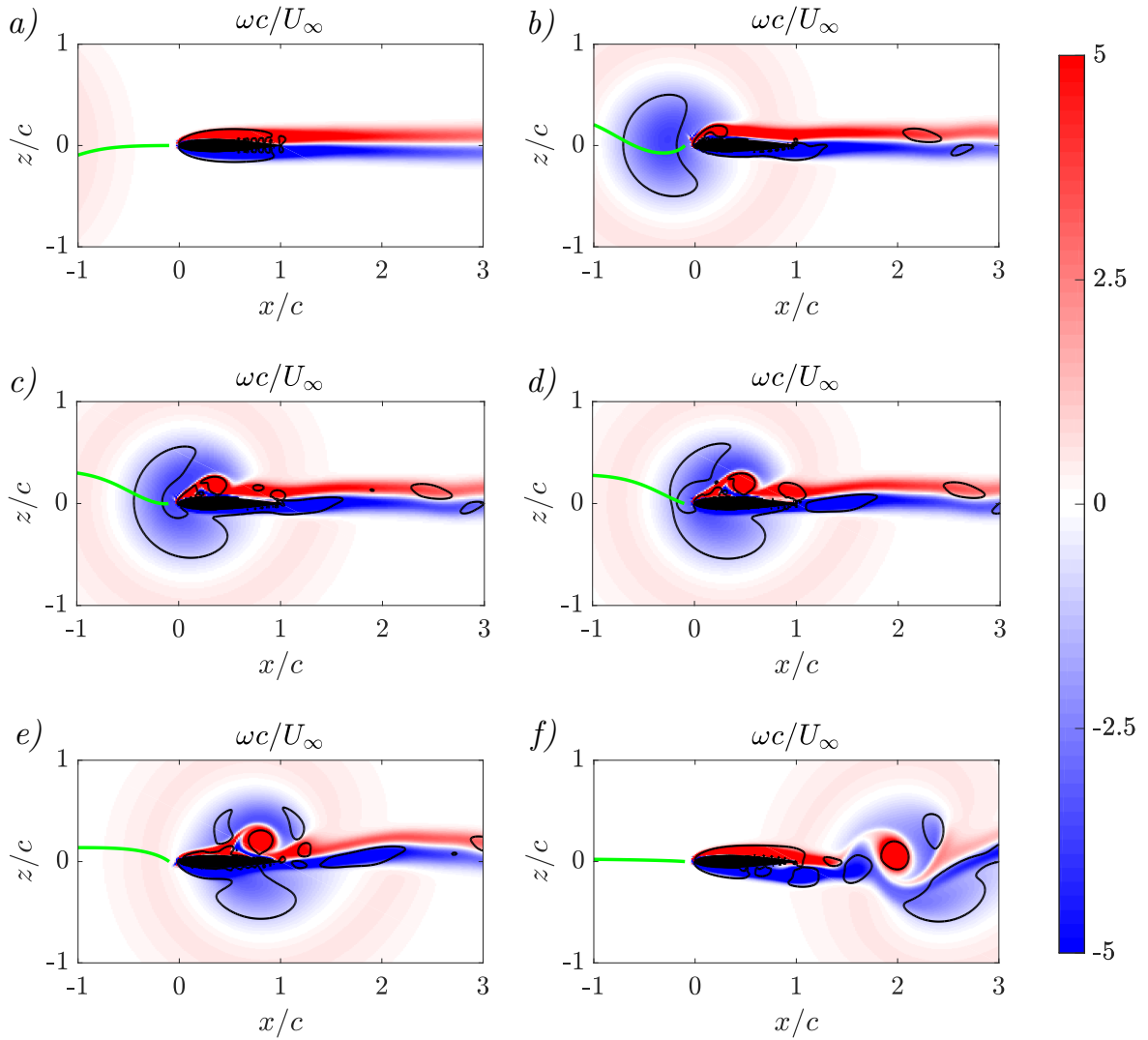


Figure 3: Vorticity contours for A0Z0D1V1 at (a) $tU_\infty/c = -2$, (b) $tU_\infty/c = -0.3$, (c) $tU_\infty/c = 0$, (d) $tU_\infty/c = 0.2$, (e) $tU_\infty/c = 0.7$, (f) $tU_\infty/c = 2.2$. The green line corresponds to the streamline arriving at $(x, z) = (-0.1c, 0)$. The black line corresponds to $\lambda_2 = -0.25U_\infty^2/c^2$.

and vortices generated in the separation of the lower-surface boundary layer are being shed into the wake, straining the remains of the vortical gust. It is interesting to note that the flow evolution depicted in figure 3 is qualitatively similar to that shown in [21, 23] and [4] at much higher Reynolds numbers. Also, similar flow structures are observed in the cases run with Lamb-Oseen vortices, as discussed later in section 3.2 (see figure 13).

The vorticity fields and effective angle of attack shown in figure 3 is consistent with the expected time evolution of the aerodynamic forces on the airfoil. This is confirmed in figure 4, which shows the time evolution of the lift coefficient C_l , the drag coefficient C_d and the effective angle of attack α_e for case A0Z0D1V1. The effective angle of attack is defined somewhat arbitrarily as the angle between the chord of the airfoil and the direction of the velocity vector at a position $0.1c$ upstream of its leading edge (i.e., same point used to defined the green streamlines shown in figure 3). Note that α_e only represents the local orientation of the flow with respect to the airfoil in the vicinity of the leading edge.

The time evolution of C_l and α_e (figure 4a and c) shows positive peaks for $t < 0$ as the vortical gust approaches the leading edge, and a negative peaks for $t > 0$ as the gust sweeps the airfoil. Note that the positive peak of C_l is larger in absolute value than the negative peak, consistent with the intensity of the peaks in the α_e and the absence of a strong LEV in the lower surface of the airfoil, as discussed in the previous paragraph. This weaker $C_{l,min}$

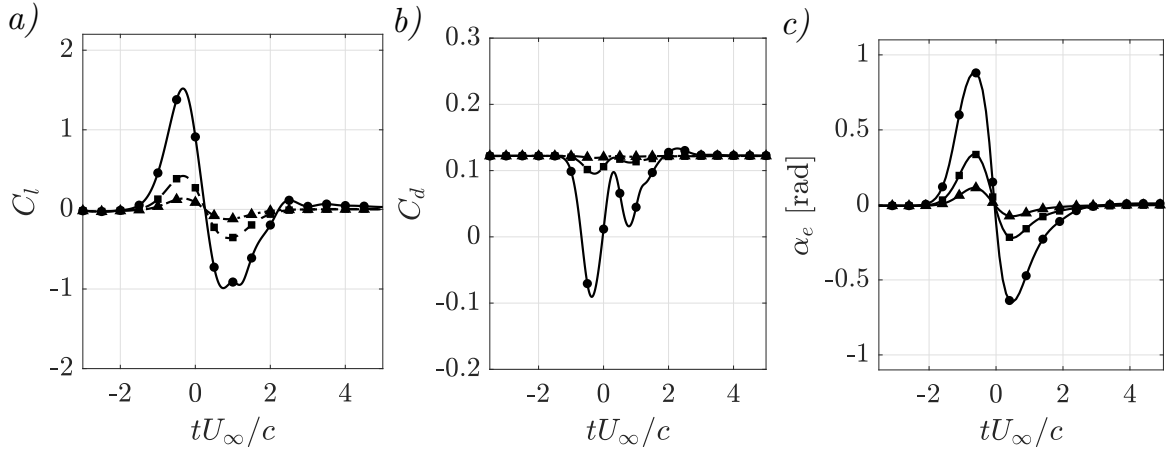


Figure 4: Temporal evolution of (a) lift and (b) drag forces, and (c) effective angle of attack for A0Z0D1. Symbols correspond to: \blacktriangle : $v_{\theta m}/U_\infty = 0.1$. \blacksquare : $v_{\theta m}/U_\infty = 0.3$. \bullet : $v_{\theta m}/U_\infty = 1.0$.

can be partly explained by the additional suction force produced by the LEV in the upper surface (observable in the pressure fields, not shown here), which partially counteracts the expected negative lift while it remains over the airfoil (i.e., for $0 < t \lesssim c/U_\infty$). This counteracting effect is absent during the initial interaction between the vortical gust and the airfoil (i.e., $t < 0$), when the boundary layer on the lower surface of the airfoil has not developed an LEV.

The evolution of the drag coefficient is shown in figure 4b, with two minima for C_d occurring nearly at the time instants where C_l is either maximum or minimum. Inspection of the pressure fields (not shown here) suggests that these drag-reduction events are due to the suction peaks generated at the leading edge when the effective angle of attack is either maximum or minimum (see α_e in figure 4c and flow visualizations in figures 3b and e). Similar reductions in drag have been reported in pitching-heaving motion [18], and flapping motion [10].

Figure 4 also includes the time histories of C_l , C_d and α_e for cases with decreasing intensity of the vortical gust (i.e, decreasing $v_{\theta m}$). The corresponding vorticity visualizations are provided in the Supplementary Material S1, S2 and S3. It can be observed that the behaviour is qualitatively the same irrespective of $v_{\theta m}$: maximum (C_l, α_e) and minimum C_d around $tU_\infty/c = -0.3$, minimum (C_l, α_e) and a second minimum C_d around $tU_\infty/c = 0.7$, slow recovery afterwards. From a quantitative point of view, the absolute value of the peaks of C_l , C_d and α_e increases monotonically with $v_{\theta m}$, suggesting that stronger vortical gusts results in larger effective angles of attack, and consequently larger aerodynamic forces. The changes in α_e and in the force coefficients also have a footprint in the vortical structures of the flow. Figure 3 shows that the vortical gust with $v_{\theta m} = 0.3U_\infty$ yields weaker vorticity perturbations in the boundary layers around the airfoil, and a strongly reduced vortex shedding into the wake.

The absence of strong LEVs could explain the similar amplitude of the maximum and minimum values of C_l and α_e for case A0Z0D1V03. Recall the previous discussion about the effect of the upper surface LEV on the negative peak of C_l for $t > 0$. Applied to case A0Z0D1V03, it would imply that C_l depends on the instantaneous angle of attack induced by the vortical gust, and not on the instantaneous positions of the LEVs (which are too weak to have an impact on C_l). From this point of view, the response of case A0Z0D1V03 is more linear, or quasi-steady.

The effect of the size of the vortical gust on the histories of C_l , C_d and α_e is evaluated in figure 6, where cases with $\alpha = 0^\circ$, $h/c = 0$, $v_{\theta m}/U_\infty = 1$ and $D/c = 0.5, 1$ and 2 are shown. The corresponding vorticity visualizations are provided in the Supplementary Material S4, S1 and S5. It can be observed that the size of the vortical gust has an impact on both

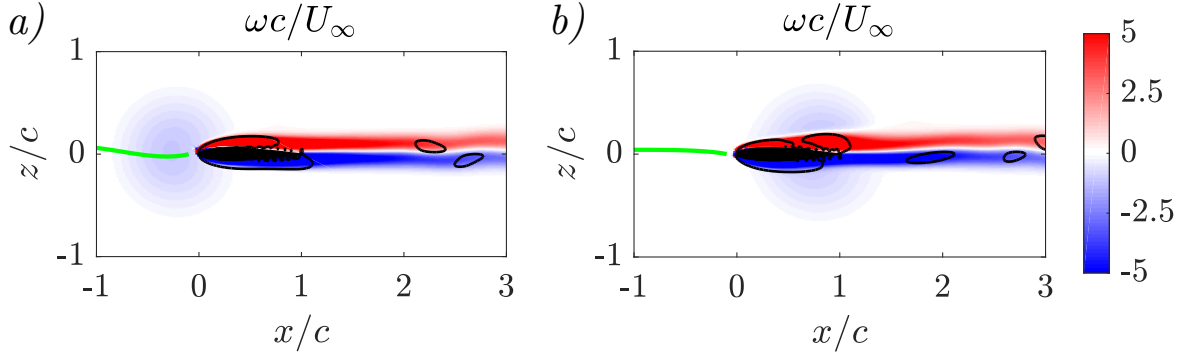


Figure 5: Vorticity contours for A0Z0D1V03 at (a) $tU_\infty/c = -0.3$, (b) $tU_\infty/c = 0.7$. The green line corresponds to the streamline arriving at $(x, z) = (-0.1c, 0)$. The black line corresponds to $\lambda_2 = -0.25U_\infty^2/c^2$.

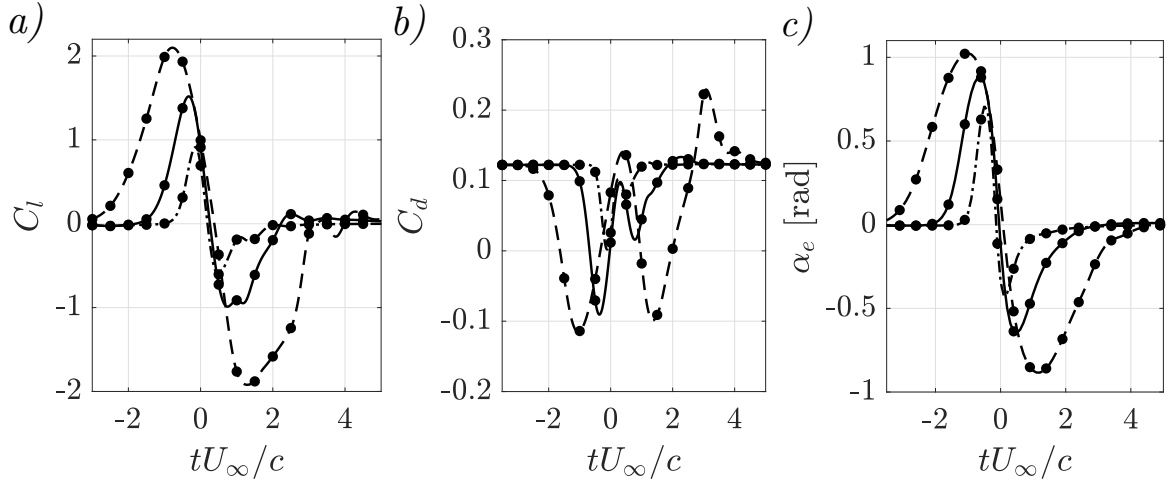


Figure 6: Temporal evolution of (a) lift and (b) drag forces, and (c) effective angle of attack for A0Z0V1. Linetypes correspond to: $-\cdot-\cdot-$: $D/c = 0.5$. $—$: $D/c = 1.0$. $-\cdot-\cdot-$: $D/c = 2.0$.

the temporal extent and the intensity of the interaction. For the largest vortical gust, the effect on the aerodynamic forces and effective angle of attack is felt earlier and last longer, the intensity of the resulting aerodynamic forces is larger (specially for the C_l), and the relaxation to the steady state is more complex, with alternating peaks of small amplitude in C_l for $t \gtrsim 3$.

The fact that the absolute value of the peaks of C_l and C_d increase monotonically with D , together with the effect of $v_{\theta m}$ discussed in figure 4, suggests that the important parameter in terms of predicting the intensity of these peaks is the circulation of the vortical gust, as suggested by the potential theory model developed by [1]. The results in figures 4 and 6 also suggests that the relationship between C_l and α_e might not be independent on the gust intensity: increasing $v_{\theta m}/U_\infty$ from 0.1 to 0.3 yields a 2-fold increase in $C_{l,\max}$ and $\alpha_{e,\max}$ (figure 4), but increasing D/c from 0.5 to 2 yields a 2-fold increase in $C_{l,\max}$ and a 1.5-fold increase in $\alpha_{e,\max}$ (figure 6). These issues will be investigated further in sections 3.2 and 3.3.

Next, the effect of the vertical distance (h) between the airfoil and the vortical gust is analyzed, keeping the size and intensity of the latter constant. The corresponding histories of C_l , C_d and α_e are shown in figure 7. The corresponding vorticity visualizations are provided in the Supplementary Material S1, S6 and S7. As h increases, the maximum values of C_l and α_e decreases monotonically, with essentially no variation on the time of the peaks. It is interesting to note that, while the negative peaks of α_e vary monotonously with h the same

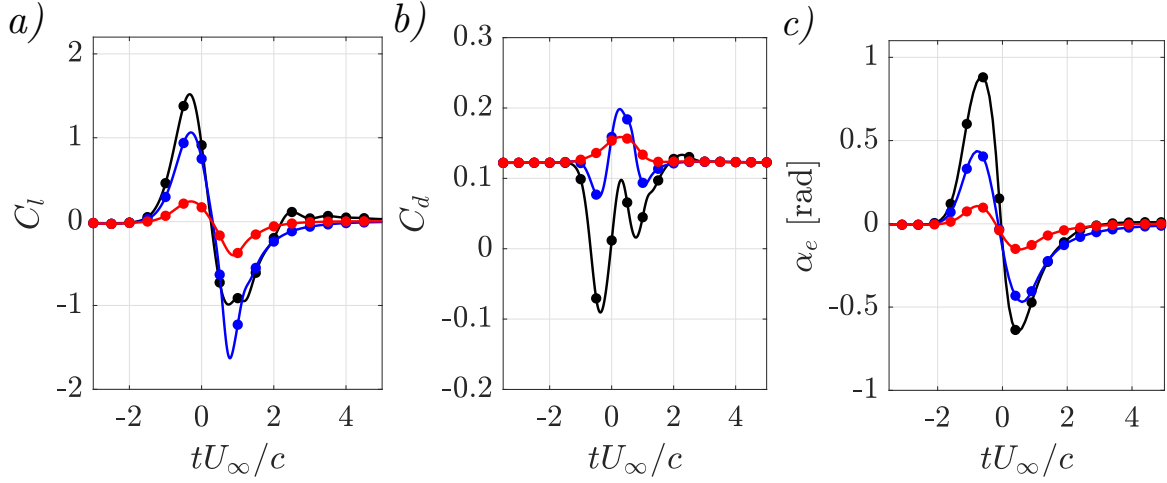


Figure 7: Temporal evolution of (a) lift and (b) drag forces, and (c) effective angle of attack for A0D1V1. Line colors correspond to: —: $h/c = 0.0$. —: $h/c = 0.5$. —: $h/c = 1.0$.

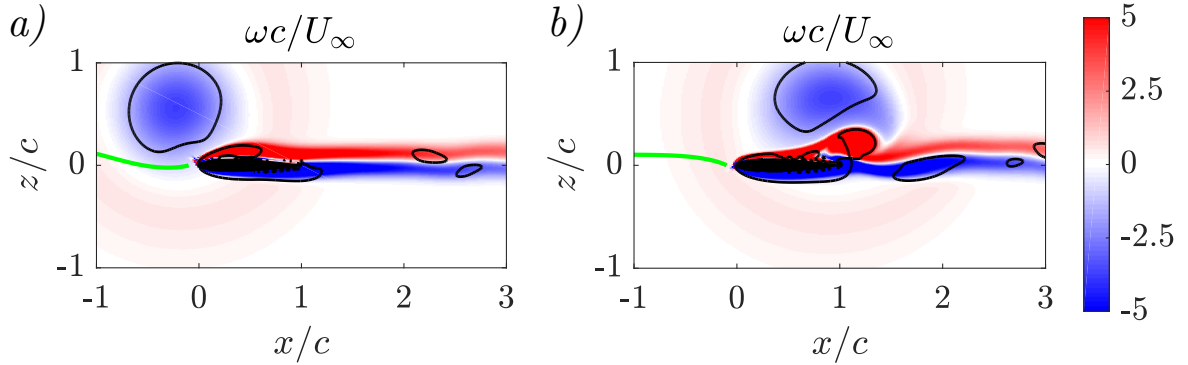


Figure 8: Vorticity contours for A0Z05D1V1 at (a) $tU_\infty/c = -0.3$, (b) $tU_\infty/c = 0.7$. The green line corresponds to the streamline arriving at $(x, z) = (-0.1c, 0)$. The black line corresponds to $\lambda_2 = -0.25U_\infty^2/c^2$.

is not true for the negative peaks of C_l . Indeed, the strongest negative C_l is observed for the case with $h/c = 0.5$.

The non-monotonous behaviour of the negative peak of C_l with h can be explained comparing the flow visualizations of cases A0Z0D1V1 and A0Z05D1V1, shown in figures 3 and 8, respectively. The most striking difference between the vorticity fields of both cases at $tU_\infty/c = 0.7$ (figures 3e and 8b) is the position of the LEV developed on the upper surface of the airfoil, which is still over the airfoil for the case with $h = 0$ but downstream of the trailing edge for the case with $h/c = 0.5$. This difference is caused by the streamwise velocities induced by the vortical gust on the upper surface of the airfoil when $h/c = 0.5$, which advect the LEV faster downstream. As it can be observed in the pressure fields shown in figure 9a, the low pressure region associated to the LEV in case A0Z0D1V1 is producing a positive contribution to C_l , and hence reducing the absolute value of the negative C_l peak at $tU_\infty/c = 0.7$. For case A0Z05D1V1 (figure 9b), the LEV and its associated low pressure region are downstream of the airfoil, and do not affect much the aerodynamic forces.

In terms of the effect of h on the drag of the airfoil, figure 7b shows that increasing h results in weaker drag-reduction with respect to static values (i.e., higher values of C_d throughout the gust). Indeed, for $h/c = 1$ drag is increased with respect to the steady state value during the whole interaction with the vortical gust. This effect is probably the result of a decrease of the intensity of the suction peak at the leading edge (due to the reduction in the effective angle of attack) combined with an increase of the skin friction drag in the upper surface of the airfoil (due to the additional horizontal velocity induced by the vortex

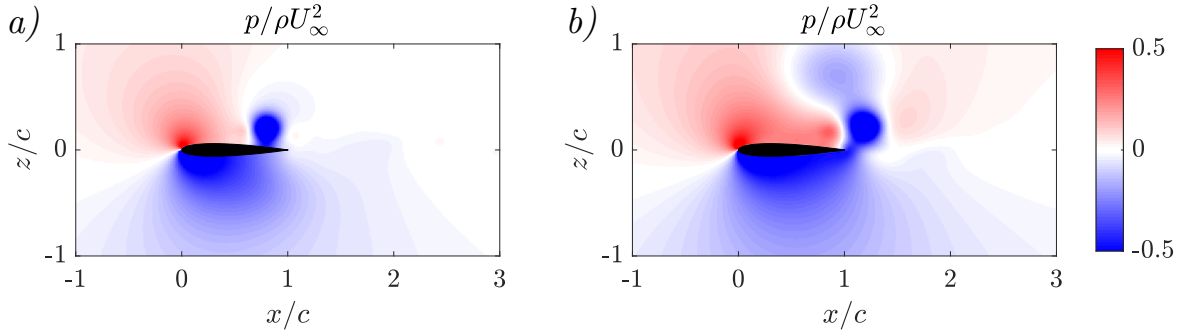


Figure 9: Pressure contours at $tU_\infty/c = 0.7$ for (a) A0Z0D1V1, (b) A0Z05D1V1.

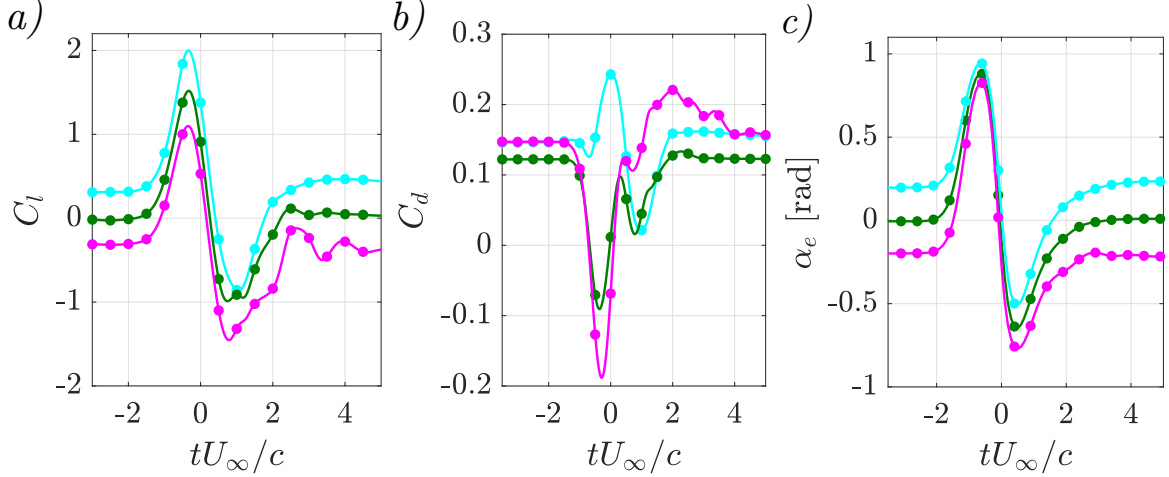


Figure 10: Temporal evolution of (a) lift and (b) drag forces, and (c) effective angle of attack for Z0D1V1. Line colors correspond to different angles of attack. —: $\alpha = -8^\circ$. —: $\alpha = 0^\circ$. —: $\alpha = 8^\circ$.

on the airfoil).

Finally, the effect of the angle of attack on the response of the airfoil to the vortical gust is evaluated in figures 10 and 11, where cases with $h/c = 0$, $D/c = 1$, $v_{\theta m}/U_\infty = 1$ and different α 's are compared. **The corresponding vorticity visualizations are provided in the Supplementary Material S8, S1 and S9.** In terms of the lift coefficient, figure 10a shows that as α increases, the evolution of $C_l(t)$ is shifted upwards. Indeed, when the difference between the instantaneous C_l and its static value is analyzed (i.e., ΔC_l , plotted in figure 11a), the effect of α on the absolute value of the maximum and minimum peaks is very small, similar to previous observations in [12] or [6]. The effect of α is more apparent on the evolution of ΔC_l in the recovery phase, with stronger oscillations for $\alpha = -8^\circ$ than for $\alpha = 0^\circ$ or 8° .

In terms of the drag coefficient, α affects both C_d and ΔC_d , as shown in figures 10b and 11b. In any case, the effect of α on C_d or ΔC_d is $\lesssim 0.3$, same order of magnitude as the differences in $\Delta C_{l,max}$ that appear in figure 11a. Indeed, the changes in ΔC_d due to α can be explained taking into account the projection of the forces induced by the vortical gust along the x -direction. As α increases, the lift force resulting from the generation of the LEV in the upper surface is tilted backwards, resulting in an increased drag. On the contrary, for $\alpha = -8^\circ$ this lift force is tilted forward, yielding a force along the negative x -axis that results in a stronger drag decrease than when $\alpha = 0^\circ$ (where the drag decrease is only due to the suction at the leading edge).

Finally, the effect of the angle of attack of the airfoil in the effective angle of attack is shown in figure 10c. First, the steady values of the α_e (i.e., for $tU_\infty/c \lesssim -2$ and for $tU_\infty/c \gtrsim 4$) are roughly 45% larger than the value of the angle of attack of the airfoil, emphasizing the fact that α_e characterizes the direction of the flow close to the leading edge,

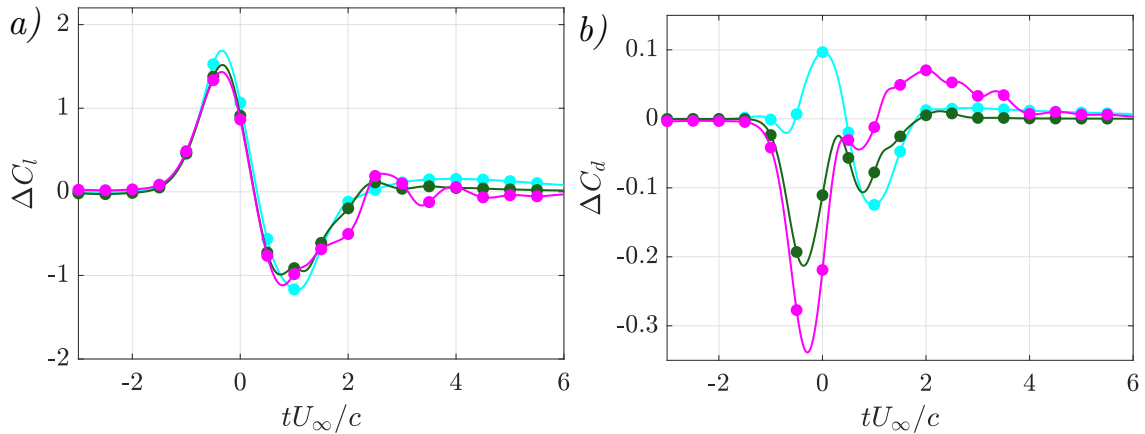


Figure 11: Temporal evolution of increments of (a) lift and (b) drag forces with respect to steady state values, for Z0D1V1. Line colors correspond to different angles of attack. —: $\alpha = -8^\circ$. —: $\alpha = 0^\circ$. —: $\alpha = 8^\circ$.

and not the direction of the free-stream with respect to the airfoil’s chord. Second, the maximum of α_e is roughly insensitive to α , consistent with the weak effect that α has on the ΔC_l in figure 11a. The same is not true for the minimum of α_e , which varies monotonously with α .

The analysis here presented is in agreement with the trends observed in previous studies at much higher Reynolds numbers [21, 23, 4].

3.2 Comparison of viscous vortical gusts with potential flow theory.

From the point of view of modeling, it is interesting to evaluate to what extent the potential theory is able to model the forces on the airfoil due to the vortical gust presented in 3.1. To that end, the potential model described in [1] is applied to the present configuration. This potential model uses Milne-Thomson circle’s theorem and conformal mapping, modelling the vortical gust as a point vortex travelling downstream and interacting with a flat plate. The circulation of the vortex remains constant during this interaction, while the bound circulation of the flat plate varies. The trajectory of the vortex is given by a system of ODEs (which must be solved numerically), and forces on the plate (i.e, its bound circulation) can be computed analytically once the instantaneous location of the vortex is known. It should be noted that the main differences between the assumptions of the potential theory model and the conditions simulated here are the low-Reynolds number ($Re = 1000$ vs a virtually infinite Reynolds number in the potential theory), the viscous nature of the vortex (with the differences in the v_θ profiles shown in figure 2), and the finite thickness of the airfoil vs an infinitely thin flat plate. Additionally, the radius of the viscous vortex considered here is $r_{vc} \sim O(c)$, while the potential theory relies on $r_{vc}/c \ll 1$.

Figure 12a shows the time evolution of ΔC_l for Taylor, Lamb-Oseen and potential vortices, for cases with $\alpha = 0^\circ$, $v_{\theta m}/U_\infty = 1$ and $D/c = 1$. Note that ΔC_l is plotted versus the streamwise position of the vortical gust with respect to the leading edge of the airfoil, which for the present viscous vortices (Taylor and Lamb-Oseen) is just $X_l(t) = tU_\infty$. Also, the circulation of the Taylor vortex is estimated at the radius of maximum v_θ (as done in [1] when comparing the potential model with the experimental results), resulting in $\Gamma = \Gamma_{v_{\theta \max}} = v_{\theta m} D \pi \exp(-1/2)$. If we focus on the first positive peak in ΔC_l , it can be observed that there is no clear agreement between the viscous and potential cases. However, both Taylor and Lamb-Oseen vortices show similar behavior when the vortex is close to the airfoil, at least in terms of the time to maximum ΔC_l and in the transition from $\Delta C_l > 0$ to $\Delta C_l < 0$. Indeed, the instantaneous vorticity fields of Taylor and Lamb-Oseen vortices for case A0Z0D1V1 (see figure 13) show that similar vortical structures are formed during the interaction between the viscous vortices and the airfoil. It is possible to see that both

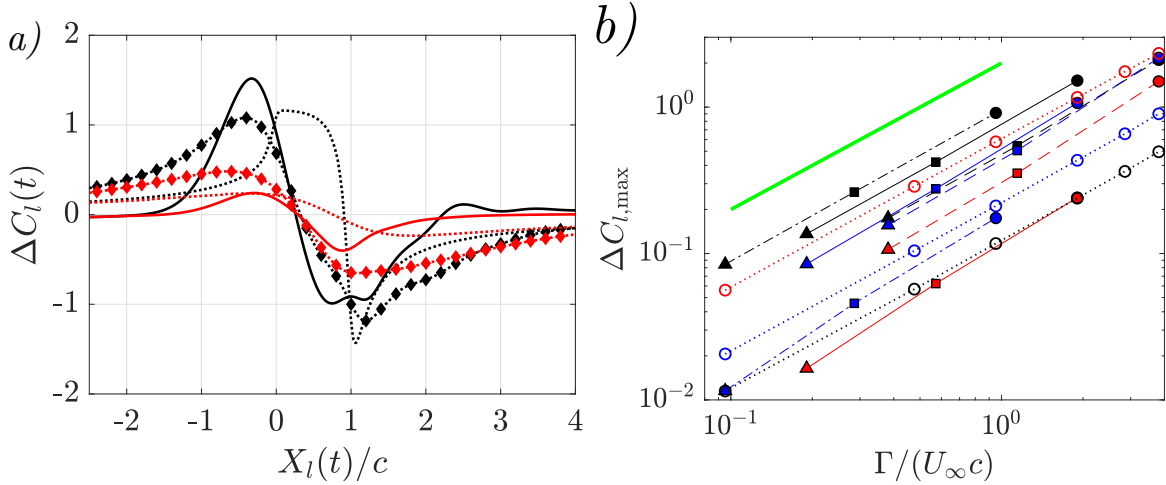


Figure 12: (a) Evolution of ΔC_l with the streamwise position of the vortical gust ($X_l(t)/c$), for Taylor (—), Lamb-Oseen (\blacklozenge), and Potential vortices (\cdots). All cases have $\alpha = 0^\circ$, $D/c = 1$, $v_{\theta m}/U_\infty = 1$ and $\Gamma = \Gamma_{v_{\theta, \max}}$. The line color indicates the value of h/c , as in table 1: —: $h/c = 0.0$. —: $h/c = 1.0$. (b) Variation of $\Delta C_{l, \max}$ with the non-dimensional circulation, at $\alpha = 0^\circ$. Taylor vortices are coded to indicate D/c and h/c , using the linetypes and colors specified in table 1. Dotted lines with open circles correspond to results from the potential model, colored with h/c (as in table 1). The solid green line on the top is $\Delta C_{l, \max} = \Gamma/(U_\infty c)$.

$v_{\theta m}/U_\infty = 0.1$	\blacktriangle	$D/c = 0.5$	$-\cdot-\cdot-$	$h/c = 0$	—
$v_{\theta m}/U_\infty = 0.3$	\blacksquare	$D/c = 1.0$	—	$h/c = 0.5$	—
$v_{\theta m}/U_\infty = 1.0$	\bullet	$D/c = 2.0$	$---$	$h/c = 1$	—

Table 1: Linetypes and symbols used for Taylor vortices at $\alpha = 0^\circ$.

vorticity and the effective angle of attack for Lamb-Oseen cases are lower, justifying the lower value for the peaks in ΔC_l compared with Taylor vortices in figure 12a. Note also that the effect of the Lamb-Oseen and potential vortices on the ΔC_l of the airfoil is evident when the vortices are relatively far from the airfoil, while the effect of the Taylor vortex is only felt at distances of the order of D . Finally, the potential theory predicts a negative peak of ΔC_l that increases in magnitude monotonously with h/c , while in the case of the viscous vortical gust this variation is not monotonous, due to the effect of h/c on the advection velocity of the LEV generated in the upper surface (discussed in section 3.1). Similar results are obtained for other values of D and $v_{\theta m}$.

The poor performance of the potential model to predict $\Delta C_{l, \max}$ in the present case contrasts with the relatively good agreement reported in [1] between experiments and the potential theory for $h \lesssim c$ and small angles of attack. The comparison between potential, Taylor and Lamb-Oseen vortices suggests that the reason for the present mismatch is related to the differences in the v_θ profile of viscous and potential vortices at small r , i.e. within the viscous core of the vortex. Indeed, the experiments agreeing with the potential model in [1] were performed at a larger Reynolds number ($Re \approx 24000$), resulting in smaller viscous cores than those considered here: the reported value of the radius to maximum circumferential velocity in the experiments is $r_{vc} = 0.07c$, while the present vortical gusts have $r_{vc} = D/2 = [0.25 - 1]c$. As a consequence, we conjecture that the viscous cores of the vortices in the experiments of [1] are weakly affected by the interaction with the airfoil, analogous to the constant circulation vortices of the potential model. On the other hand, in the present simulations the vortical gusts are modified in the interaction with the airfoil, provided they are strong enough. This can be observed in the λ_2 contours presented in figures 3, 8 and 13.

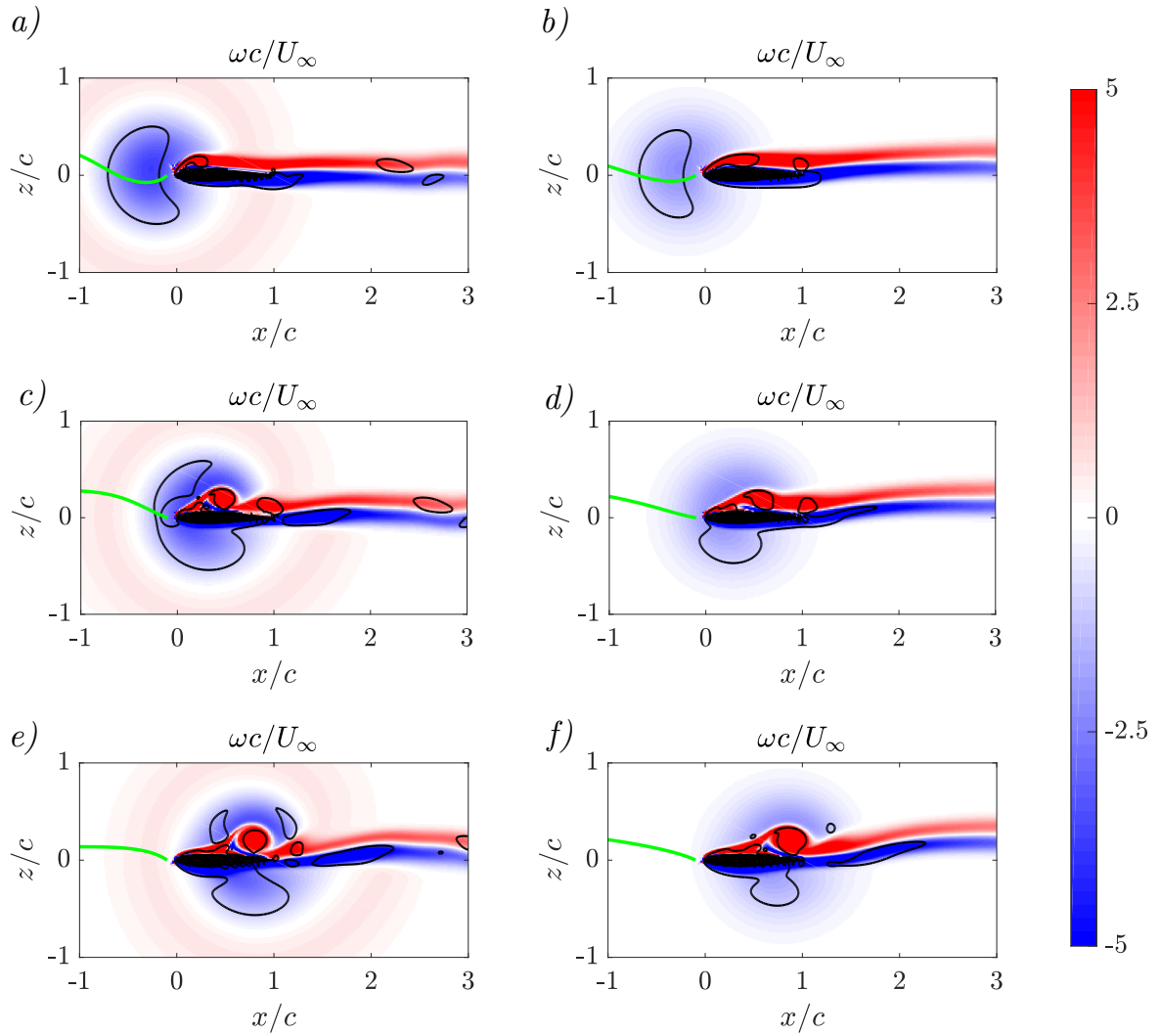


Figure 13: Vorticity fields for Taylor Vortex (left) and Lamb-Oseen Vortex (right) with A0Z0D1V1 at $tU_\infty/c = -0.3$ (top), $tU_\infty/c = 0.2$ (mid) and $tU_\infty/c = 0.7$ (bottom). The green line corresponds to the streamline arriving at $(x, z) = (-0.1c, 0)$. The black line corresponds to $\lambda_2 = -0.25U_\infty^2/c^2$.

Weaker vortical gusts seem less affected by the airfoil, like case A0Z0D1V03 (see figure 5).

Besides these differences, the DNS results show that $\Delta C_{l,\max}$ is roughly proportional to the circulation of the vortical gust, as predicted by the potential model. This is shown in figure 12b, where all cases with $\alpha = 0^\circ$ are presented. The line types and symbols used in the figure for the Taylor vortices are reported in table 1. The results of the potential model for $h/c = 0, 0.5$ and 1 are also included in the figure with open symbols. It can be observed that for viscous vortical gusts at given values of $\Gamma/(U_\infty c)$ and $h/c = 0$, the resulting $\Delta C_{l,\max}$ varies up to a factor of 2 when D/c varies from 0.5 to 2. This variability, which is not captured by the potential model, becomes greater as h increases.

3.3 A semi-empirical model for lift response to viscous vortical gusts

Based on the results presented in the previous sections, it is clear that for the viscous vortical gusts considered in the present study the resulting $\Delta C_l(t)$ depends on the intensity of the vortical gust (i.e., its circulation), the vertical distance to the airfoil and the size of the vortical gust. Note that the potential model does not include the latter, but assumes that $r_{vc} \ll c$. As a consequence, the potential model is flawed when the radius of the viscous core of the vortex is not much smaller than the airfoil chord.

Previous works on transverse gusts [19, 24] have shown that the peak values of the lift coefficient due to the gust (i.e., $\Delta C_{l,\max}$) are roughly proportional to the maximum effective angle of attack, defined as the ratio between the maximum vertical velocity of the gust over the free-stream velocity. Similar observations were made by [10] when comparing heaving and flapping wings. Hence, it seems reasonable to test how well does $\alpha_{e,\max}$ characterizes $\Delta C_{l,\max}$ in the present configurations, even if the effective angle of attack in transverse gusts is *global* (i.e., it is felt by the whole airfoil) while the definition of $\alpha_e(t)$ used here is *local* (i.e., only represents the flow direction near the leading edge).

This test is performed in figure 14, where $\Delta C_{l,\max}$ is plotted as a function of $\alpha_{e,\max}$. Figure 14a only shows results for $\alpha = 0^\circ$, while figure 14b shows results for $\alpha = -8^\circ, 0^\circ$ and 8° . The solid lines in both panels correspond to linear fits for $\Delta C_{l,\max}(\alpha_{e,\max})$, with $R^2 = 0.8895$, $R_{adjusted}^2 = 0.8851$, and $RMSE = 0.217$ for figure 14a and $R^2 = 0.8871$, $R_{adjusted}^2 = 0.8856$, and $RMSE = 0.2097$ for figure 14b. Even if the linearity between $\Delta C_{l,\max}$ and $\alpha_{e,\max}$ approximately holds, there is considerable variation at a given $\alpha_{e,\max}$ depending on the values of D/c , h/c and α (i.e., a factor of two or more). Indeed, similar fits can be obtained for $\sin(\alpha_{e,\max})$, without any significant improvement over the results presented in figure 14. This variability was already anticipated in section 3, and it might be related to the *local* character of $\alpha_{e,\max}$ discussed above. Also, it is important to note that $\alpha_{e,\max}$ is not a parameter that is known *a priori*: it is a result of a (relatively costly) DNS simulation, and hence has a limited value in terms of a predictive model for vortical gusts.

In the remaining of this section we propose an alternative empirical model, that overcomes the limitations of the potential model and the scaling of $\Delta C_{l,\max}$ with $\alpha_{e,\max}$. This empirical model is based on scaling the lift coefficient with an *averaged* effective angle of attack that can be estimated *a priori* (i.e., without solving a DNS), and on normalizing the time over which ΔC_l peaks with the size of the vortical gust. These two parameters (averaged effective angle of attack and proper time scale) completely characterize the effect of the vortical gust on the aerodynamic forces on the airfoil, capturing the influence of $v_{\theta m}$, D and h .

First of all, the results presented in section 3 suggest that the time at which ΔC_l peaks (namely, t_{\max}) depends mostly on the diameter of the viscous vortex (see figure 6), with little effect of $v_{\theta m}$ (i.e., figure 4), h (i.e., figure 7) and α (i.e., figure 10). This idea is also supported by the results of the potential model, since the ΔC_l of the potential vortices (with $D \rightarrow 0$) peak at $X_l(t)/c = 0$ (i.e., $tU_\infty/c = 0$), as shown in figure 12(a). Figure 15a shows the time to peak as a function of D/c for all the cases in the present database, including Taylor and Lamb-Oseen vortices. Remember that $t = 0$ corresponds to the time at which the center of the viscous vortex would reach the position of the leading edge of the airfoil, if the airfoil were not present. The figure shows that t_{\max} is approximately a linear function of D/c .

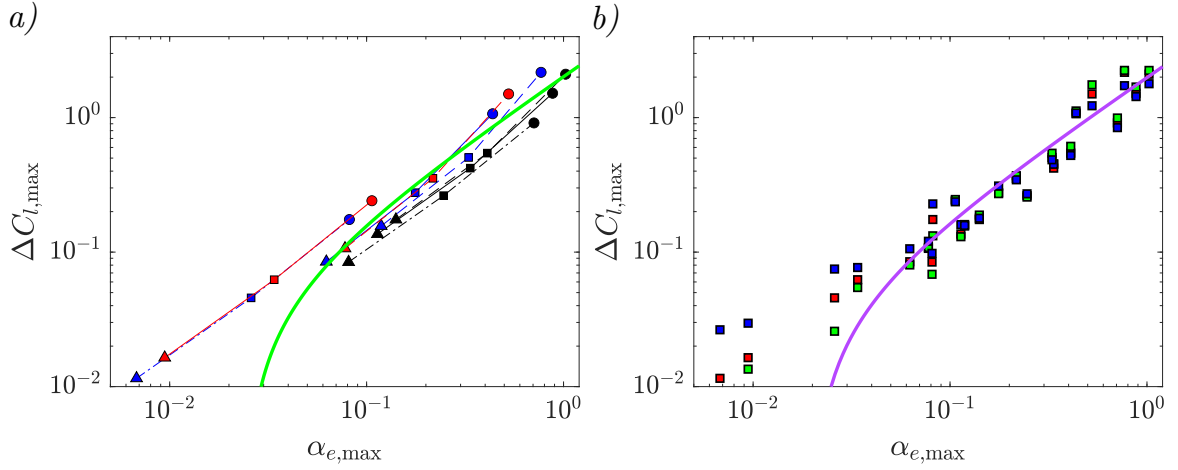


Figure 14: Maximum ΔC_l as a function of the maximum effective angle of attack $\alpha_{e,\max}$ induced by the vortex on the airfoil in logarithmic scale. (a) Taylor vortices for $\alpha = 0^\circ$. Lines and colors as indicated in table 1. (b) Taylor vortices for different angles of attack (—: $\alpha = 8^\circ$; —: $\alpha = 0^\circ$; —: $\alpha = -8^\circ$). Green (—) and purple (—) lines correspond to fittings (a) using only cases with $\alpha = 0^\circ$ and (b) using cases with $\alpha = -8^\circ, 0^\circ, 8^\circ$.

Indeed, the agreement of the data from Taylor vortices to linear regression lines (computed independently for each value of α) is reasonably good for most of the data. The regression lines for $\alpha = 0^\circ$ and 8° coincide (red and green dashed lines), whereas the regression line for $\alpha = -8^\circ$ (in blue dashed line) is slightly different. Most of the outliers at $D/c = 1$ seem to correspond to $\alpha = -8^\circ$. The linear fit between t_{\max} and D/c also seems to work reasonably well for the Lamb-Oseen vortices when $h/c = 0$ and 0.5 (black and blue diamonds in figure 15a collapsing on top of each other), but not for the Lamb-Oseen vortex at $h/c = 1$ (red diamond on figure 15a).

Figure 15b shows t_{\max} versus the circulation of the vortical gusts for Taylor and Lamb-Oseen vortices with $\alpha = 0^\circ$. The data for the Taylor vortices appear clustered in horizontal lines, each line corresponding to a value of D/c , although with some scatter for cases with $\Gamma/(U_\infty c) \gtrsim 2$. The Lamb-Oseen vortices have $D/c = 1$, and consequently we can observe that they fall close to the Taylor vortices with $D/c = 1$, at least for $h/c = 0$ and 0.5 . Again, the Lamb-Oseen vortex with $h/c = 1$ presents a different behaviour, with a value of t_{\max} closer to the largest Taylor vortices ($D/c = 2$).

Figure 15a also shows a linear regression line to the whole database (black dashed line), which corresponds to

$$t_{\max} U_\infty / c = -0.4033 D/c + 0.06997, \quad (8)$$

with $R^2 = 0.9718$, $R^2_{\text{adjusted}} = 0.9714$ and $RMSE = 0.0427$.

The second piece of the alternative empirical model proposed here is the *averaged* effective angle of attack. Unlike $\alpha_e(t)$ defined in section 3, the idea is to provide an effective angle of attack that can be computed *a priori* and that captures the *global* effect of the vortical gust on the airfoil. Hence, we choose to work with the spatial average of the vertical velocity induced by the vortex over the airfoil chord, namely w_h . This average is computed when the vortical gust is at x_{\max} , which corresponds to the streamwise position where ΔC_l peaks. For the Taylor vortex, this results in

$$w_h = \frac{1}{c} \int_0^c v_{\theta m} \frac{2(x - x_{\max})}{D} \exp\left(-\frac{2r^2}{D^2}\right) dx, \quad (9)$$

where $r = \sqrt{(x - x_{\max})^2 + h^2}$ and $x_{\max} \approx U_\infty t_{\max}$. The latter assumes a constant advection velocity of the vortical gust at velocity U_∞ , and requires estimating t_{\max} using equation (8). Note that w_h depends on the vortex intensity, size and vertical displacement of the

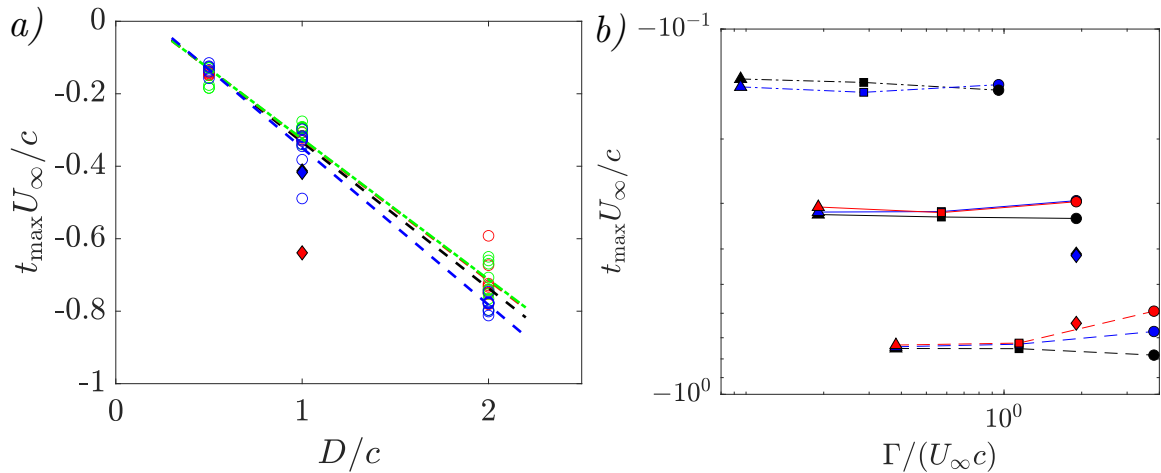


Figure 15: (a) Time for maximum ΔC_l , as a function of the diameter of the viscous gust. Taylor vortices are represented by empty circles, colors indicating the angle of attack (—: $\alpha = 8^\circ$; —: $\alpha = 0^\circ$; —: $\alpha = -8^\circ$). Dashed lines correspond to the linear regressions for each angle of attack. (b) Time for maximum ΔC_l , as a function of the circulation of the vortex, for $\alpha = 0^\circ$. Taylor vortices are represented with the lines and symbols reported in table 1, and their circulation is defined as $\Gamma = \Gamma_{v_{\theta, \max}}$. In both panels, Lamb-Oseen vortices are represented with diamonds colored with h/c (\blacklozenge : $h/c = 0.0$; \blacklozenge : $h/c = 0.5$; \blacklozenge : $h/c = 1.0$).

vortical gust, and can be estimated *a priori*, without running a simulation or performing an experiment.

Figure 16 shows $\Delta C_{l, \max}$ as a function of w_h/U_∞ in logarithmic (a,b) and linear scales (c,d), for $\alpha = 0^\circ$ (a,c) and $\alpha = -8^\circ, 0^\circ, 8^\circ$ (b,d). The figures also include a linear regression curve (in cyan) given by

$$\Delta C_{l, \max} = 4.076 \cdot w_h/U_\infty - 0.00317. \quad (10)$$

This curve has been obtained fitting all Taylor vortices, resulting in a linear regression with $R^2 = 0.9748$, $R^2_{\text{adjusted}} = 0.9744$ and $\text{RMSE} = 0.0991$, **which has a smaller scatter than $\Delta C_{l, \max}$ versus $\alpha_{e, \max}$ in figure 14.**

Figure 16 shows that equation (10) adjust the Taylor vortices moderately well at all α . The small deviations observed for $w_h/U_\infty \lesssim 10^{-2}$ correspond to small vortices ($D/c = 0.5$) relatively far from the airfoil ($h/c \geq 0.5$), as it can be observed in 16a for the $\alpha = 0^\circ$ case. On the other hand, the small deviations observed for the largest values of w_h correspond to cases with $v_{\theta m} = U_\infty$, as it can be observed in figure 16c for case $\alpha = 0^\circ$.

It is worth noting that the main trends observed in figure 16 are observed for other *a priori* estimations of the effective angle of attack of the airfoil, like the velocity induced by the vortex at $x = c/4$ (not shown). However, the scatter of the results is smaller for the integral definition of w_h given in equation (9).

The relative good fit provided by equations (8) and (10), together with the similar shapes of the time evolutions of $C_l(t)$ shown in figures 4, 6, 7 and 10, raises the question of whether it is possible to obtain a self-similar evolution for ΔC_l . To that end, we compute ensemble averages of $\Delta C_l/(w_h/U_\infty)$ as a function of tU_∞/D^1 for the cases with Taylor vortices and $w_h/U_\infty > 0.01$. These are shown in figure 17a, together with the corresponding medians and the 10% and 90% percentiles, for all Taylor vortices irrespective of the angle of attack.

Inspection of figure 17a shows that mean and median coincide until the peak in ΔC_l is reached, meaning that the statistical distribution is symmetric. Besides, the 10% and 90% percentile curves remain close to the mean value. In that sense, it is possible to conclude that the initial response of NACA0012 airfoils to Taylor vortices is self-similar. After $\Delta C_{l, \max}$ is reached, mean and median begin to deviate from each other, while the distance between

¹Note that this is equivalent to t/t_{\max} , since t_{\max} is proportional to D/U_∞ .

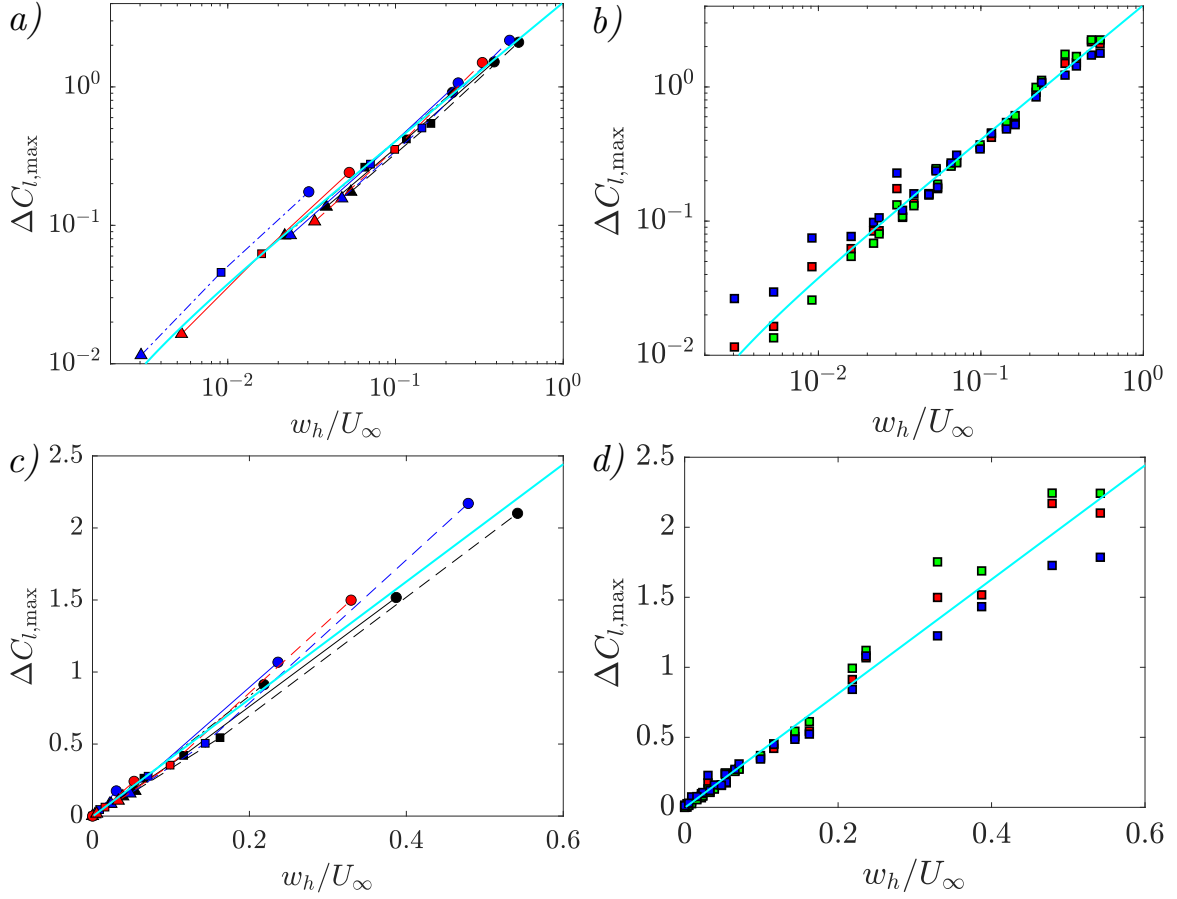


Figure 16: Maximum ΔC_l as a function of the averaged vertical velocity induced by the vortex on the airfoil, w_h/U_∞ . (a,b) in logarithmic scale, and (c,d) in linear scale. (a,c) Taylor vortices for $\alpha = 0^\circ$. Lines and colors as indicated in table 1. (b,d) Taylor vortices for different angles of attack (—: $\alpha = 8^\circ$; —: $\alpha = 0^\circ$; —: $\alpha = -8^\circ$). In all panels the cyan line (—) corresponds to equation (10).

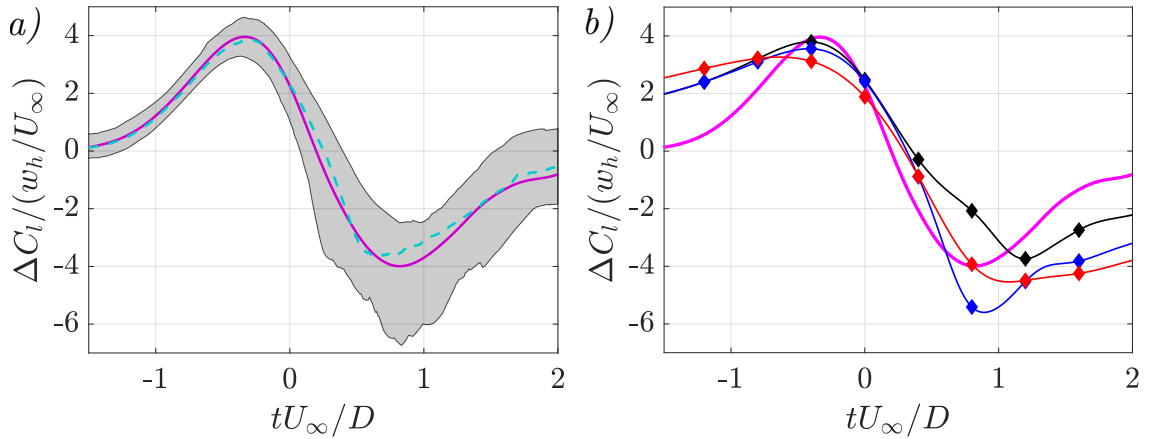


Figure 17: Evolution of $\Delta C_l / (w_h / U_\infty)$ as a function of tU_∞ / D . (a) Mean (—), median (---), 10% and 90% percentiles (shaded areas) obtained from all cases with Taylor vortices. (b) Mean value for Taylor vortices (—), compared to instantaneous evolutions for Lamb-Oseen vortices (\blacklozenge : $h/c = 0.0$; $\blue\lozenge$: $h/c = 0.5$; $\red\lozenge$: $h/c = 1.0$).

the 10% and 90% percentiles increases. This suggests that the self-similar scaling is less valid for $t > 0$, mainly due to the non-linear interactions between Taylor vortex, LEVs and the boundary layers of the airfoil.

Figure 17b compares the self-similar evolution of $\Delta C_l / (w_h / U_\infty)$ of the Taylor vortices (given by its mean value) to the evolutions of $\Delta C_l / (w_h / U_\infty)$ of the three Lamb-Oseen vortices considered in this work. For the latter, w_h is estimated using the velocity profile given in equation (3), and the expression for t_{\max} given in equation (8). Overall, Taylor and Lamb-Oseen evolutions do not agree, with the latter showing a much slower build up of $\Delta C_l / (w_h / U_\infty)$ for $t < 0$. This is consistent with the slower decay of the circumferential velocity profiles of Lamb-Oseen vortices, which would result in stronger long-distance interactions than in Taylor vortices. Besides these differences, it is worth noting that the peak values of $\Delta C_l / (w_h / U_\infty)$ for Taylor and Lamb-Oseen vortices agree reasonably well (i.e., approximately within the 10% and 90% percentiles of Taylor vortices, as shown in figure 17a). The Lamb-Oseen vortices with $h/c = 0.5$ and $h/c = 0$ collapse on top of each other during the initial evolution of the gust ($t < 0$), but show significant differences in the evolution for $t > 0$. The Lamb-Oseen vortex with $h/c = 1$ has a significantly different evolution, peaking at earlier times than $h/c = 0.5$ and 0 . This suggests that, provided with the necessary DNS data, a self-similar evolution for $\Delta C_l / (w_h / U_\infty)$ could also be computed for Lamb-Oseen vortices, albeit with a different shape as that obtained for Taylor vortices.

4 Conclusions

The effect that vortical (viscous) gusts have on the aerodynamic forces of a NACA0012 airfoil has been analyzed using direct numerical simulations at low Reynolds number ($Re = 1000$). The Reynolds number considered here is consistent with the range of vortex diameters chosen for the study ($D/c = 0.5 - 2$), corresponding to viscous cores with sizes comparable to the airfoil chord. A large database is presented and discussed, with 81 simulations of Taylor vortices (varying the size D , maximum circumferential velocity $v_{\theta m}$, vertical distance of the vortical gust h , and angle of attack of the airfoil α) and 3 additional simulations for Lamb-Oseen vortices.

In agreement with previous works **at higher Reynolds numbers**, a negative (counterclockwise) vortical gust produces an initial increase in the lift coefficient as it approaches the airfoil ($t < 0$), followed by a negative perturbation in C_l as it sweeps the airfoil and interacts with the airfoil wake ($t > 0$). The angle of attack seems to have a small effect on the perturbation of the aerodynamic force, so that the change in the lift coefficient ΔC_l

remains fairly independent on the angle of attack. The intensity of the initial positive perturbation of ΔC_l increases with the size (D) and intensity of the vortical gust ($v_{\theta m}$), and decreases when the vertical displacement (h) of the vortical gust with respect of the airfoil increases. The behaviour of the negative peak of ΔC_l at $t > 0$ is not monotonous with the vertical displacement of the vortex, due to the interactions between the vortical gust and the Leading Edge Vortex (LEV) developed during the initial interaction of the gust and the airfoil.

The interactions of the airfoil with Taylor and Lamb-Oseen vortices are qualitatively similar. However, due to the slower decay of the velocity profiles induced by the latter, the effect of Lamb-Oseen vortices is felt in the aerodynamic forces of the airfoil at larger distances than for Taylor vortices. As a consequence, head-on Lamb-Oseen vortices ($h/c = 0$) have a progressive effect on the airfoil that results in somewhat weaker LEVs and lower peaks of ΔC_l compared to Taylor vortices. On the other hand, when $h/c \sim 1.0$, Lamb-Oseen vortices have a stronger effect on the aerodynamic response of the airfoil than Taylor vortices.

Special attention has been paid to the characterization of the peak value in the lift coefficient perturbation ($\Delta C_{l,\max}$) with the parameters of the gust. Contrary to potential models, where $\Delta C_{l,\max}$ depends only on the vortex circulation ($\Gamma \propto Dv_{\theta m}$) for a fixed vertical displacement (h), the present data show that ΔC_l for a viscous gust at a fixed h is not a linear function of the circulation of the gust (i.e., $v_{\theta m}D$), **but has an explicit dependency on D** . However, by defining and averaged vertical velocity induced by the vortical gust (w_h), we have been able to show empirically that $\Delta C_{l,\max} \approx 4w_h/U_\infty$ for all viscous vortices considered here (Taylor and Lamb-Oseen). By definition, w_h depends on the intensity, size, velocity profile and vertical displacement of the gust. Moreover, it can be estimated *a priori*, without having to run a simulation or a experiment: only the velocity profile of the vortical gust is needed.

Finally, the scaling of $\Delta C_{l,\max}$ with w_h can also be applied to the initial development of $\Delta C_l(t)$, resulting in a single function $\Delta C_l/(w_h/U_\infty) = f(tU_\infty/D)$ characterizing the growth of ΔC_l for a given vortical gust velocity profile. Note that in the previous expression, w_h and tU_∞/D capture the effect of the intensity ($v_{\theta m}$), size (D) and vertical distance (h) on the perturbation of the lift coefficient. The effect of the velocity profile of the viscous vortical gust (i.e., Taylor vortex, Lamb-Oseen vortex, etc.) is captured in the shape of the function $f(tU_\infty/D)$. This result is particularly interesting, and **its extension to higher Reynolds numbers, airfoil geometries and to other models for vortical gusts is left for future works**.

Acknowledgements

This work was partially supported by grant DPI2016-76151-C2-2-R (AEI/FEDER, UE). We thank Dr. García-Villalba for fruitful discussions.

References

- [1] J. Alaminos-Quesada and R. Fernández-Feria. Effect of the angle of attack on the transient lift during the interaction of a vortex with a at plate. potential theory and experimental results. *J. Fluid. Struct.*, 74:131–141, 2017.
- [2] G. Arranz, A. Gonzalo, M. Uhlmann, O. Flores, and M. García-Villalba. A numerical study of the flow around a model winged seed in auto-rotation. *Flow, Turbul. Combust.*, 101(2):477–497, 2018.
- [3] G. Arranz, M. Moriche, M. Uhlmann, O. Flores, and M. García-Villalba. Kinematics and dynamics of the auto-rotation of a model winged seed. *Bioinspir. Biomim.*, 13(3):036011, 2018.

- [4] C.J. Barnes and M.R. Visbal. Counterclockwise vortical-gust/airfoil interactions at a transitional reynolds number. *AIAA J.*, 56(7):2540–2552, 2018.
- [5] C.J. Barnes and M.R. Visbal. Gust response of rigid and elastically mounted airfoils at a transitional reynolds number. *Aerosp. Sci. Technol.*, 74:112–119, 2018.
- [6] H. Biler, C. Badrya, and A.R. Jones. Experimental and computational investigation of transverse gust encounters. *AIAA J.*, pages 1–15, 2019.
- [7] H. Chen and J.W. Jaworski. Aeroelastic interactions and trajectory selection of vortex gusts impinging upon joukowski airfoils. *J. Fluid. Struct.*, 96:103026, 2020.
- [8] S.J. Corkery and H. Babinsky. An investigation into gust shear layer vorticity and the added mass force for a transverse wing-gust encounter. In *AIAA Scitech 2019 Forum*, page 1145, 2019.
- [9] S.J. Corkery, H. Babinsky, and J.K. Harvey. On the development and early observations from a towing tank-based transverse wing-gust encounter test rig. *Exp. Fluids*, 59(9):135, 2018.
- [10] A. Gonzalo, G. Arranz, M. Moriche, M. García-Villalba, and O. Flores. From flapping to heaving: A numerical study of wings in forward flight. *J. Fluid. Struct.*, 83:293–309, 2018.
- [11] J.H. Horlock. Fluctuating lift forces on aerofoils moving through transverse and chord-wise gusts. *J. Basic. Eng.*, 90(4):494–500, 1968.
- [12] E.A.L. Hufstedler and B.J. McKeon. Vortical gusts: Experimental generation and interaction with wing. *AIAA J.*, 57(3):921–931, 2019.
- [13] J. Jeong and F. Hussain. On the identification of a vortex. *J. Fluid Mech.*, 285:69–99, 1995.
- [14] H.G. Küssner. Zusammenfassender bericht über den instationären auftrieb von flügeln. *Luftfahrtforschung*, 13(12):410–424, 1936.
- [15] J.M. Leung, J.G. Wong, G.D. Weymouth, and D.E. Rival. Modeling transverse gusts using pitching, plunging, and surging airfoil motions. *AIAA J.*, 56(8):3271–3278, 2018.
- [16] M. Moriche. *A numerical study on the aerodynamic forces and the wake stability of flapping flight at low Reynolds number*. PhD thesis, Universidad Carlos III Madrid, 2017.
- [17] M. Moriche, O. Flores, and M. García-Villalba. Three-dimensional instabilities in the wake of a flapping wing at low reynolds number. *Int. J. Heat. Fluid Fl.*, 62:44–55, 2016.
- [18] M. Moriche, O. Flores, and M. Garcia-Villalba. On the aerodynamic forces on heaving and pitching airfoils at low reynolds number. *J. Fluid Mech.*, 828:395–423, 2017.
- [19] M. Moriche, A. Gonzalo, O. Flores, and M. Garcia-Villalba. Fast transverse maneuvers at low reynolds numbers. In *AIAA Scitech 2019 Forum*, page 0640, 2019.
- [20] T.J. Mueller and J.D. DeLaurier. Aerodynamics of small vehicles. *Annu. Rev. Fluid Mech.*, 35(1):89–111, 2003.
- [21] L. Nguyen, V. Golubev, and M.R. Visbal. Numerical study of transitional sd7003 airfoil interacting with canonical upstream flow disturbances. *AIAA J.*, 56(1):158–181, 2018.
- [22] D. Peng and J.W. Gregory. Vortex dynamics during blade-vortex interactions. *Phys. Fluids*, 27(5):053104, 2015.

- [23] D. Peng and J.W. Gregory. Asymmetric distributions in pressure/load fluctuation levels during blade-vortex interactions. *J. Fluid. Struct.*, 68:58–71, 2017.
- [24] G. Perrotta and A.R. Jones. Unsteady forcing on a flat-plate wing in large transverse gusts. *Exp. Fluids*, 58(8):101, 2017.
- [25] G. Perrotta and A.R. Jones. Quasi-steady approximation of forces on flat plate due to large-amplitude plunging maneuvers. *AIAA J.*, 56(11):4232–4242, 2018.
- [26] H. Press and B. Mazelsky. A study of the application of power-spectral methods of generalized harmonic analysis to gust loads on airplanes. 1954.
- [27] D.E. Raveh and A. Zaide. Numerical simulation and reduced-order modeling of airfoil gust response. *AIAA J.*, 44(8):1826–1834, 2006.
- [28] D. Tang and E.H. Dowell. Experimental and theoretical study of gust response for high-aspect-ratio wing. *AIAA J.*, 40(3):419–429, 2002.
- [29] M. Uhlmann. An immersed boundary method with direct forcing for the simulation of particulate flows. *J. Comp. Phys.*, 209(2):448–476, 2005.
- [30] P. Zehner, F. Falissard, and X. Gloerfelt. Aeroacoustic study of the interaction of a rotating blade with a batchelor vortex. *AIAA J.*, pages 629–647, 2018.